Optimized Switching Finite Control Set Model Predictive Control of NPC Single-Phase Three-Level Rectifiers

Xu Zhang, Guojun Tan, *Member, IEEE*, Tao Xia, Qiang Wang, and Xiang Wu

***Abstract*—A new model predictive control scheme, optimized switching finite control set model predictive control, is studied in this article for neutral-point-clamped (NPC) single-phase three-level pulsewidth modulation (PWM) rectifiers. To ensure the actual stability of the power converter, the ac-side current error of single-phase PWM rectifier and the neutral point voltage of the converter are both converged to the bounded invariant set, and the adjustment of system performance is thus realized by setting the bounded invariant set. Based on the NPC single-phase three-level PWM rectifier model, the ac-side current, the neutral point voltage, and the current error in the future time can be predicted in advance. The above objectives are achieved by optimizing the selection of switch combinations. The advantage of the proposed method is that it can reduce the average switching frequency of the converter when the ac-side current error and the neutral point voltage of the converter are controlled within a certain range, which makes it suitable for the application of high-power single-phase PWM rectifier.**

***Index Terms*—Finite control set, model predictive control, single-phase PWM rectifier, three level.**

I. Introduction

SINGLE-PHASE pulsewidth modulation (PWM) rectifiers play an important role in industrial applications, especially in high-power applications such as the high-speed railway traction drive system [1]. These converters are called active front end rectifiers, which realize the bidirectional power flow, while maintaining the high power factor (PF) and the low-harmonic current distortion [2], [3].

Single-phase three-level PWM rectifiers perform better than two-level rectifiers in terms of voltage classes, power density, and current harmonic characteristic. Hence, single-phase three-level PWM rectifiers are widely used in the field of railway locomotive traction. At present, there are many system control schemes such as *dq*-axis current control [2], proportional-resonant current control [3], direct power control (DPC) [4], model predictive DPCs [5], deadbeat control [6], etc. However, the available literature shows that for the above methods, they all need carrier modulation to achieve current or power tracking. In railway locomotive applications with high power and low switching frequency, the discrete period is equal to the switching period, i.e., the carrier period. Therefore, the discrete accuracy of the system is reduced at low switching frequencies.

J. Rodriguez [7] proposed a scheme of finite control set model predictive control (FCS-MPC). Owing to its excellent performance in terms of nonlinear control, multiobjective optimization, dynamic response and precision, it has been studied extensively in many fields, such as high-voltage direct current transmission [8], wind power generation [9], induction motor control [10], inverter power supply [11], and permanent magnet synchronous motor [12], etc. Compared with the method that requires carrier modulation, the discrete period of FCS-MPC algorithm is much smaller than its average switching period, so the discrete accuracy of the system is higher at low switching frequencies and has a wide application prospect in the field of low-switching frequency and high power [13].

Moreover, the FCS-MPC algorithm for the control of the single-phase PWM rectifier is studied in [14]. In [15], the FCS-MPC is further studied by controlling the neutral-point-clamped (NPC) single-phase three-level PWM rectifier and the dc-side voltage prediction link is introduced to improve the dynamic performance of the system. However, the cost function only takes into account grid-current tracking and the neutral-point voltage deviation, without considering the effect of switching frequency.

It is worth noting that although FCS has the ability of multiobjective optimization, there are still many uncertainties in its multiple-objective weight factors selection methods and stability analysis [16] and [19]. In addition, the selection of weight factors are generally based on the offline test results [20]. As have been studied in [16]–[20], the weighting factors has large influences on the control performance of power electronic control system, and it is also quite difficult to design. Therefore, completely eliminating it is a better way to reduce its influences on the control system.

In [21], a predictive torque and flux control for induction motors powered by a three-phase two-level voltage source converter is studied. A multiobjective ranking based strategy is proposed. The torque and flux linkage errors are ordered separately. The

Manuscript received July 4, 2019; revised September 26, 2019, November 25, 2019, and January 15, 2020; accepted February 21, 2020. Date of publication March 6, 2020; date of current version June 23, 2020. This work was supported in part by the National Key R&D Program of China Award 2016YFC0600804 and in part by the National Natural Science Foundational of China under Award U1610113. Recommended for publication by Associate Editor D. Neacsu. *(Corresponding author: Guojun Tan.)*

The authors are with the School of Electrical and Power Engineering, China University of Mining and Technology, Xuzhou 221008, China (e-mail: lnyk_zhangxu@163.com; gjtan_cumt@163.com; gjtan@cumt.edu.cn; gsts_xiatao@163.com; 04141547@cumt.edu.cn; cumtwuxiang@cumt.edu.cn).

Color versions of one or more of the figures in this article are available online at http://ieeexplore.ieee.org.

Digital Object Identifier 10.1109/TPEL.2020.2978185

voltage vectors with lower values are assigned a lower ranking, while the voltage vectors with higher values are assigned a higher ranking. Then, the voltage vector output that minimizes the average ranking is selected for control. Therefore, the tuning of weighting factors is unnecessary. The literature [22] applied the multiobjective banking based strategy to a permanent magnet synchronous motor powered by a matrix converter to achieve good dynamic and steady-state performance. In [23], both the torque and the stator flux control errors are transformed into dynamic per-unit values, which are the same order of magnitude. Next, a new dynamic cost function is proposed on the basis of the two dynamic per-unit values, which does not require weighting factor anymore. In [24], proposed method realizes the optimizations for the torque and flux cost function terms simultaneously. This approach constrains the torque and the stator flux tracking errors within the bounds. The torque error boundary is dynamically adjusted so that there are 2–4 voltage vectors that satisfy the torque error within the boundary, and the stator flux boundary is also obtained in the same way. Then, the voltage vector that satisfies both the torque and the stator flux error within the above boundary can be selected as a system output by a certain rule. Thereby the weight coefficients are eliminated and have good parameter robustness.

In [25]–[27], the references of stator flux magnitude and torque in conventional model predictive torque control (MPTC) are converted into an equivalent reference of stator flux vector. As only the tracking error of stator flux vector is required in the cost function, the use of weighting factor is eliminated. The literature [28] converts the reference value of the stator flux and torque in the conventional MPTC into an equivalent reference of the stator flux vector. The stator flux linkage error and the number of switching times corresponding to different voltage vectors are sorted, and the switching frequency is reduced by multiobjective ranking based strategy. The literature [29] sorts the torque error, stator flux error, and switching times of different voltage vectors, respectively, and adopts multiobjective ranking based strategy. When the average ranking is the same, the voltage vector with the least number of switching times is selected, which reduces the switching frequency. However, the literature [28], [29] switching frequency cannot be adjusted according to the designer's needs. For the NPC single-phase three-level PWM rectifier, it is difficult to obtain a direct mathematical relationship between the balance control of the midpoint potential and the current error and switching frequency. In the literature [30], for the T-type three-level converter, the midpoint potential balance is controlled by the redundant switch state, but the switching frequency is not optimally controlled.

The research results in [31] show that the controlled targets of two-level converter cannot converge to the required steady-state value, but the actual stability of the power converter can be guaranteed by converging these variables to a bounded invariant set. The theoretical analysis of the weight coefficients selection of the two-level converter using FCS-MPC algorithm is carried out in [31]. However, there is not a method to determine the weighting factor to ensure system stability for more complex power converter topologies, which makes the optimization scheme by translating the multiobjective optimization problem into the use of weighting factors to unify multiple control objectives into a single cost function limited [32].

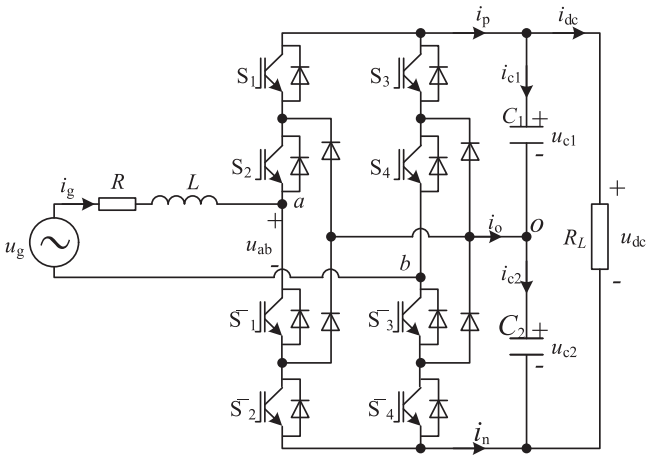

Fig. 1. Single-phase three-level NPC converter.

In this article, a control scheme optimized switching finite control set model predictive control (OS-FCS-MPC) for the NPC single-phase three-level PWM rectifier is proposed. First, the conventional FCS-MPC algorithm is studied to establish a cost function including current error, the neutral-point voltage deviation, and switching frequency limit. Then, the method of converging the current error and the neutral-point voltage deviation to the bounded invariant set is proposed to ensure the actual stability of the power converter. Finally, a comparison between conventional FSC-MPC and the proposed control method in terms of the current harmonic characteristic, the average switching frequency, the neutral-point voltage deviation, and system parameter design. Simulation and experimental results show the effectiveness and superiority of the proposed scheme.

II. Single-Phase PWM Rectifier Mathematical Model

A. AC-Side Current Prediction Model

Fig. 1 shows the topology of a single-phase three-level neutral point-clamped converter, where the continuous-time dynamic of the grid-current i_g is shown as

$$\frac{di_g}{dt} = \frac{1}{L}(u_g - Ri_g - u_{ab}). \tag{1}$$

In (1), u_g represents the grid-voltage, u_{ab} stands for the input voltage of the adopted converter, L is the grid-side filter inductor, and R is the parasitic resistance. The voltage of capacitors in the dc link is shown as (2), where i_{C1}, i_{C2}, and i_p, i_n are respectively the capacitor currents and internal currents of the adopted converter, $i_{\rm dc}$ represents the dc-link current

$$\begin{cases} \dfrac{du_{C1}}{dt} = \dfrac{1}{C_1} i_{C1} = \dfrac{1}{C_1}(i_p - i_{\rm dc}) \\ \dfrac{du_{C2}}{dt} = \dfrac{1}{C_2} i_{C2} = \dfrac{1}{C_2}(-i_n - i_{\rm dc}). \end{cases} \tag{2}$$

TABLE I
SWITCHING STATES

S_1	S_2	S_3	S_4	S_A	S_B	S_{AB}	u_{ab}	states V_x
1	1	0	0	1	-1	2	$u_{C1}+u_{C2}$	V_1
1	1	0	1	1	0	1	u_{C1}	V_2
0	1	0	0	0	-1	1	u_{C2}	V_3
0	1	0	1	0	0	0	0	V_4
1	1	1	1	1	1	0	0	V_5
0	0	0	0	-1	-1	0	0	V_6
0	1	1	1	0	1	-1	$-u_{C1}$	V_7
0	0	0	1	-1	0	-1	$-u_{C2}$	V_8
0	0	1	1	-1	1	-2	$-u_{C1}-u_{C2}$	V_9

In (2), C_1 and C_2 are the dc-side upper and lower bus capacitance values, respectively. To realize the prediction of the grid-current, the forward Euler method is adopted to transform (1) into a discrete-time form, i.e.,

$$i_g^{k+1} = \left(1 - \frac{T_s R}{L}\right) i_g^k + \frac{T_s}{L}(u_g^k - u_{ab}^k) \tag{3}$$

where T_s is the sampling period and according to the adopted switching states in Table I, u_{ab} can be expressed as

$$u_{ab}^k = u_{C1}^k(S_1 - S_3) + u_{C2}^k(S_2 - S_4) \tag{4}$$

where $S_i(i = 1, 2, 3, 4)$ are the switching states. Therefore, i_g at the $k + 1$th instant can be predicted by the previous sampling instant of i_g, u_g, u_{C1}, and u_{C2}. Similar to the previous method used in (3), the discrete-time form of (2) can be described as

$$\begin{cases} u_{C1}^{k+1} = \dfrac{T_s}{C_1} i_p^k - \dfrac{T_s}{C_1} i_{dc}^k + u_{C1}^k \\ u_{C2}^{k+1} = -\dfrac{T_s}{C_2} i_n^k - \dfrac{T_s}{C_2} i_{dc}^k + u_{C2}^k. \end{cases} \tag{5}$$

Based on the direction relation between the switching states of the adopted converter and i_g as [15], the value of i_p and i_n can be calculated as

$$\begin{cases} i_p^k = \dfrac{S_A(S_A + 1) - S_B(S_B + 1)}{2} i_g^k \\ i_n^k = \dfrac{S_A(S_A - 1) - S_B(S_B - 1)}{2} i_g^k. \end{cases} \tag{6}$$

Consequently, according to (3) and (5), the controller can easily derive the estimated values for the predictions of the grid-current and capacitor voltages, respectively.

B. Instantaneous Power Model

As shown in Fig. 2, where u_α, u_β are the two orthogonal signals generated by second-order generalized integrator (SOGI), where u_d, u_q, i_d, i_q are d-axis and q-axis components of voltage and current in the two-phase rotating coordinate system, respectively. As shown in Fig. 2, it is assumed that the grid-voltage u_m is fixed to d-axis by PLL, namely, $u_d = u_m$ and $u_q = 0$.

Hence, according to the instantaneous power theory, the grid-current i_g can be expressed as

$$i_g^k = \frac{2p_g^k}{u_d^k}\cos\theta + \frac{2q_g^k}{u_d^k}\sin\theta \tag{7}$$

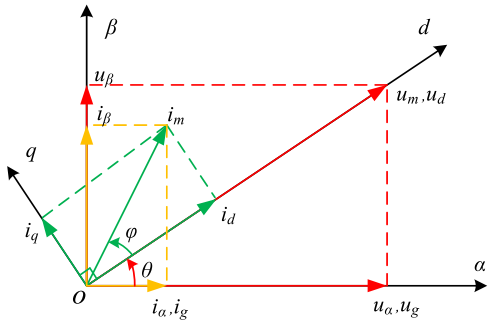

Fig. 2. Vector diagram.

where p_g^k and q_g^k are the instantaneous active power and reactive power, respectively.

Therefore, the active and reactive power injected to or absorbed from the grid can be controlled by regulating the grid-side current.

C. DC Bus Voltage Prediction Model

Obviously, the dc-link power can be expressed as

$$p_{\rm dc}^k = p_{C1}^k + p_{C2}^k + p_{Z_{\rm dc}}^k = i_p^k u_{C1}^k - i_n^k u_{C2}^k \tag{8}$$

where i_p and i_n are obtained according to (6).

Traditionally, it is impossible to compare the instantaneous values of ac power and dc power. To solve this problem, we define the dc-side average power reference as $p_{\rm dc\_av}^*$ and the ac-side average active power reference as $p_{g\_\rm av}^*$. Based on the principle of power balance, we can obtain

$$p_{g\_\rm av}^{*k+1} = p_{R\_\rm av}^{k+1} + p_{\rm dc\_av}^{*k+1} \tag{9}$$

where $p_{R\_\rm av}$ represents the filter resistor power loss.

Clearly, it is impossible to get $p_{\rm dc\_av}^*$ directly from (8). Consequently, $p_{\rm dc\_av}^*$ is derived from the average values for each item in (8). The capacitor voltage is always controlled by its current. However, due to the limitation of the properties of power electronics, the capacitor current is limited. In order to ensure that the capacitor voltages reach the expected value while maintaining power balance, a reference prediction horizon N^* is introduced.

Therefore, the future average voltage references of capacitor can be obtained according to

$$u_{\rm dc\_av}^{*k+1} = u_{\rm dc}^k + \frac{1}{N^*}(u_{\rm dc}^{*k} - u_{\rm dc}^k). \tag{10}$$

In addition, the average value of the neutral-point current i_o is approximately zero when neutral point voltage is in a dynamic equilibrium. Hence, the average capacitor current references are deduced as

$$i_{C1\_\rm av}^{*k+1} = i_{C2\_\rm av}^{*k+1} = i_{C\_\rm av}^{*k+1} = \frac{\frac{C_1 C_2}{C_1 + C_2}}{T_s}(u_{\rm dc\_av}^{*k+1} - u_{\rm dc}^k) \tag{11}$$

where C_1, C_2 represent the dc-link capacitor value. The average dc-current at this moment can be written as

$$i_{\rm dc\_av}^{*k+1} = \frac{u_{\rm dc\_av}^{*k+1}}{R_{L\_\rm av}^{*k+1}}. \tag{12}$$

As the actual values of $u_{\rm dc}^k$ can be measured and assuming that the average dc-link power consumption related to $R_{L\_\rm av}$ is a constant within two sampling periods, $R_{L\_\rm av}^{k+1}$ can be expressed as

$$R_{L\_\rm av}^{k+1} = \frac{u_{\rm dc}^k}{i_{\rm dc}^k}. \tag{13}$$

Based on the above analysis, the average dc-power reference $p_{\rm dc\_av}^{*k+1}$ is defined as (14)

$$p_{\rm dc\_av}^{*k+1} = (i_{\rm dc\_av}^{*k+1} + i_{C\_\rm av}^{*k+1})u_{\rm dc\_av}^{*k+1}. \tag{14}$$

Considering a large second-order harmonic component existed in the dc-side variables of single-phase converters, a notch-filter centered at 100 Hz (2*f*) is adopted. Moreover, the notch-filter output is used as a reference $p_{dc\_av\_2f}^{*k+1}$, which is possible to provide an ac-side current reference i_g^{*k+1} with good immunities to second-order harmonics.

In addition, it is essential to estimate the resistor power loss to get the filter inductor loss, i.e.,

$$p_{R\_\rm av}^{*k+1} = R\left(\frac{i_m^{k+1}}{\sqrt{2}}\right)^2 = \frac{R}{\left(u_m^{k+1}/\sqrt{2}\right)^2}\left((p_{g\_\rm av}^{k+1})^2 + (q_{g\_\rm av}^{k+1})^2\right) \tag{15}$$

where $u_m^{k+1} \approx u_m^k$ and i_m^{k+1} stand for the peak values of grid-voltage and current, respectively, and $q_{g\_\rm av}^{k+1}$ is the ac-side reactive power average.

According to (9), (14), and (15), the ac-side power can be calculated. Thus, (7) can be expressed as a quadratic equation of $p_{g\_\rm av}^{k+1}$

$$\frac{2R}{(u_m^k)^2}(p_{g\_\rm av}^{*k+1})^2 - p_{g\_\rm av}^{*k+1} + p_{\rm dc\_av\_2f}^{*k+1} + \frac{2R}{(u_m^k)^2}(q_{g\_\rm av}^{*k+1})^2 = 0. \tag{16}$$

The solution that minimizes the power is given by

$$p_{g\_\rm av}^{*k+1} = \frac{\rho^k}{2}\left(1 - \sqrt{1 - \frac{4}{\rho^k}\left(p_{\rm dc\_av\_2f}^{*k+1} + \frac{(q_{g\_\rm av}^{*k+1})^2}{\rho^k}\right)}\right) \tag{17}$$

where $\rho^k = \frac{(u_m^k)^2}{2R}$.

Therefore, the value of i_g^{*k+1} is obtained according to

$$i_g^{*k+1} = \frac{2p_{g\_\rm av}^{*k+1}}{u_m^k}\cos\theta + \frac{2q_{g\_\rm av}^{*k+1}}{u_m^k}\sin\theta. \tag{18}$$

III. Conventional FCS-MPC

A. Cost Function Formulation

For NPC single-phase three-level PWM rectifiers, the ac-side active and reactive power can be controlled individually by the ac-side current provided by the converter. However, the converter here also needs to maintain the dc-side capacitor voltage balance ($u_{C1} \approx u_{C2} \approx u_{\rm dc}/2$) and restrict switching frequency.

Considering that the three controlled variables (ac-side current tracking, dc-side voltage regulation, the control of switching frequency) are tightly coupled.

These control requirements can be expressed by formulas through the cost function to get the minimum value. The cost function for the NPC single-phase three-level PWM rectifier consists of the following components:

$$J_1^k = (i_g^{*k+1} - i_g^{k+1})^2 + k_c(u_{C1}^{k+1} - u_{C2}^{k+1})^2 + k_n(\left|S_A^k - S_A^{k-1}\right| + \left|S_B^k - S_B^{k-1}\right|). \tag{19}$$

In the formula, the first term is the current tracking error, the second term is the midpoint potential deviation, and the third term is the number of power electronic switch conversions. The weight factors k_c and k_n are used to handle the relationship among reference current tracking, midpoint voltage balance, and variables that contribute to switching frequency reduction. Some larger weight factors value implies a greater priority for this goal.

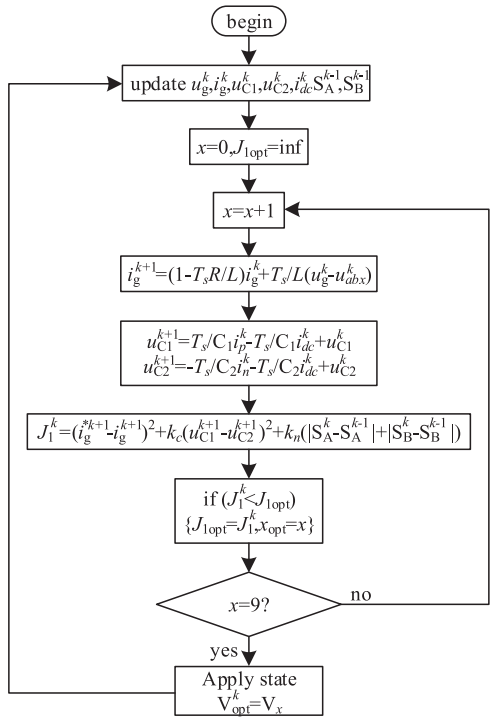

Fig. 3. Flow diagram of the conventional FCS-MPC algorithm.

B. FCS-MPC Strategy

The flow diagram of the conventional FCS-MPC algorithm is drawn as Fig. 3, where u_{abx}^k represents the u_{ab} corresponding to the switch state V_x at time *k*. Here, the outer loop is executed at every sampling time, the inner loop is executed for each possible state, obtaining the optimized switching state to be applied during the next sampling period.

The control block diagram of the conventional FCS-MPC algorithm is drawn as Fig. 4. The first step is to set required dc-voltage reference $u_{\rm dc}^{*k+1}$ and the reactive power reference $q_{g\_\rm av}^{*k+1}$ and then bring them into the dc-side voltages predictive block. Meanwhile, part of this control block inputs are the main grid parameters, i.e., peak voltage u_m^k and angle θ provided by the SOGI block. The second step is to estimate the future current reference i_g^{*k+1} using the measured values of u_g^k, i_g^k, u_{C1}^k, u_{C2}^k and $i_{\rm dc}^k$ at the instant *k* and reactive power reference

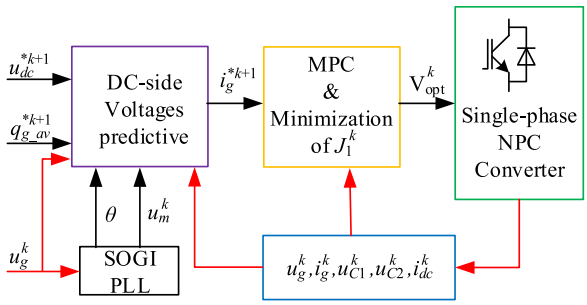

Fig. 4. Control block diagram of the conventional FCS-MPC algorithm.

q_g^{*k+1} guarantees the required power factor. After that, the third step is to figure out the optimized switching combination V_{opt}^k in Table I for obtaining the minimization of the cost function J_1^k.

IV. Optimized Switching Finite Control Set Model Predictive Control

The good performance single-phase three-level NPC converter system has high complexity due to multiple tightly coupled control targets. The key control goal is to track the dc-voltage reference and maintain high-power quality in terms of PF and total harmonics distortion (THD) on the ac side. Meanwhile, the neutral-point voltage is kept to zero to constrain voltage stress of the switches. The temperature of the switch should stay at the appropriate value. Since the limited cooling ability and system efficiency of the converter, it is necessary to contrain the switching loss to limit the temperature of the converter, which is affected by the switching frequency. Due to the limited cooling capacity of the converter, its temperature can be limited by reducing the switching losses. Besides, the switching loss of the converter is controlled by its switching frequency, indirectly. Apparently, the switching frequency can be easily measured and monitored.

The conventional FCS-MPC relies on the weighting factor to adjust the weight priority of each indicator. The scheme of multiobjective optimization based on weight factors reduces the switching frequency. Since the contradiction between the various control objectives, the weight factors design is difficult and the relation between the weight factors and the control target is difficult to quantify.

The most important thing is that improper design of the weighting factors may directly lead to system instability. For example, if the weighting factor k_n is too small, the required low switching frequency cannot be guaranteed. If the weighting factor k_n is too large, the switching state will remain unchanged, which directly causes the grid side current to fail to track the reference value, and the dc-side voltage cannot track the reference value. It may cause damage to the converter's power electronics due to overcurrent or overvoltage damage to the power electronics due to out of control of the midpoint potential. If the weighting factor k_c is too small, the midpoint potential deviation will be too large to cause overvoltage damage to the power electronics. If k_c is too large, the switching state will

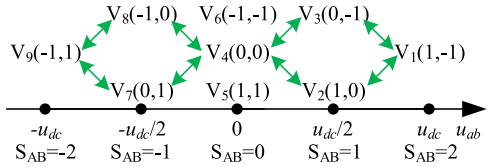

Fig. 5. Switching rules switching diagram.

TABLE II
Effect of Switching State on Midpoint Voltage

states V_x	V_2	V_3	V_7	V_8
i_g>0	↘	↗	↗	↘
i_g<0	↗	↘	↘	↗

only select V_2, V_3, V_7, and V_8 to act on the converter. It causes the grid side current and the dc-side voltage to fail to track the reference value.

This article proposes the control scheme that uses the switching state to perform switching optimization control on the qualitative relationship of each control target to reduce the switching frequency under the premise of quantitative control of the neutral point voltage deviation and grid side current error. Actually, it is impossible to guarantee that the neutral point voltage will remain at zero and the ac-side current will be absolutely sinusoidal at each sampling instant. Therefore, we set the upper and lower bounds of its reference; the switching state remains unchanged when the neutral voltage and the grid side current are kept within a certain range. If any of these references exceed the limit, they will be corrected rapidly.

A. Rule of Switch State Switching

According to Table I, there are nine switching states for the single-phase NPC three-level converter, traditionally. These switching sequences are constrained by the following conditions: 1) The switching states are absolutely not allowed to jump across level states. 2) For each cell, to ensure that the switching transition occurs at most once in each switching period. After following the above procedure, the switching rules for the single-phase three-level NPC converter can be expressed as Fig. 5.

B. Midpoint Voltage Control

Analysis (5), (6) and Table I show that only the V_2, V_3, V_7, and V_8 act on the converter, the midpoint potential changes, and the other switch states have no effect on the midpoint potential. According to (5) and (6), the switch states and the connection between ac-side current and the neutral point voltage are shown as Table II, where "↘" and "↗" represent the neutral point voltage increase and decrease, respectively.

According to Table II, it can be concluded that when $S_{AB} = \pm 1$, the midpoint voltage balance can be controlled by selecting an appropriate redundant switching state according to the grid side current and the midpoint potential.

C. Proposed OS-FCS-MPC Strategy

When the electric current error is within the given reference error range at the $k+1$th sampling period. If the current error and the midpoint potential error are within the given reference error range at the $k+1$th sampling period, the original switching state is maintained, thereby achieving a reduction in the average switching frequency. Since only $|\mathrm{S}^{k-1}_{\mathrm{AB\_opt}}| = 1$ affects the midpoint potential, when $|\mathrm{S}^{k-1}_{\mathrm{AB\_opt}}| \neq 1$, the midpoint potential does not continue to deteriorate while maintaining the original switching state. Therefore, when the current error is within the given error reference range in the k + 1th sampling period, if $|\mathrm{S}^{k-1}_{\mathrm{AB\_opt}}| \neq 1$, the original switching state is maintained. When the current error is within the given reference range at the $k+1$th sampling period, the midpoint potential error is not within the given reference error range and $|\mathrm{S}^{k-1}_{\mathrm{AB\_opt}}| = 1$, the $\mathrm{S_{AB}}$ is maintained unchanged. The switching state is selected based on the grid side current and the midpoint potential. When the current error is not within the given reference error range at the $k+1$th sampling period, the $\mathrm{S_{AB}}$ that satisfies the rule of switch state switching and minimizes the grid side current error is selected, and then the switch state is selected according to the rule of switch state switching and the midpoint potential.

In order to keep the output variables within the given limits, the proposed algorithm in this article can be expressed as follows.

Step 1: Redefine the cost function, i.e., $J_2^k = |i_g^{*k+1} - i_g^{k+1}|$, which is only related to ac-side current.

Step 2: Assuming the neutral point voltage is effectively controlled, the output u_{ab} can be estimated as $\mathrm{S_{AB}}u_{\mathrm{dc}}/2$ according to Table I.

Step 3: The current reference i_g^{*k+1} can be calculated by (18).

Step 4: Assuming $V_{\mathrm{opt}}^k = V_{\mathrm{opt}}^{k-1}$, the $k+1$th estimated current reference can be obtained according to

$$i_g^{k+1} = \left(1 - \frac{T_s R}{L}\right) i_g^k + \frac{T_s}{L}(u_g^k - S_{AB} u_{\mathrm{dc}}/2) \tag{20}$$

u_{C1}^{k+1} and u_{C2}^{k+1} will be calculated according to (4)–(6).

Step 5:

$$\text{If } |i_g^{*k+1} - i_g^{k+1}| \leq \Delta i_g, |u_{C1}^{k+1} - u_{C2}^{k+1}| \leq \Delta u_C \text{ or } |S^{k-1}_{\mathrm{AB\_opt}}| \neq 1,\ V_{\mathrm{opt}}^k = V_{\mathrm{opt}}^{k-1};$$

$$\text{If } |i_g^{*k+1} - i_g^{k+1}| \leq \Delta i_g, |S^{k-1}_{\mathrm{AB\_opt}}| = 1, |u_{C1}^{k+1} - u_{C2}^{k+1}| > \Delta u_C, S^k_{\mathrm{AB\_opt}} = S^{k-1}_{\mathrm{AB\_opt}};$$

where Δu_C is the neutral point voltage deviation reference and Δi_g is the ac-side current deviation reference.

Step 6: If $|i_g^{*k+1} - i_g^{k+1}| > \Delta i_g$, according to (20), the $k+1$th current references i_g^{k+1} at different $\mathrm{S_{AB}}$ states are calculated, and the optimal $S^k_{\mathrm{AB\_opt}}$ to minimum $J_2^k = |i_g^{*k+1} - i_g^{k+1}|$ are selected. Note that according to the rule of switch state switching, if $|S^k_{\mathrm{AB\_opt}} - S^{k-1}_{\mathrm{AB\_opt}}| > 1$, it is discarded directly.

Step 7: Switching state selection according to Table III.

TABLE III
SWITCHING STATE SELECTION

$S^k_{\mathrm{AB\_opt}}$	$(u^k_{C1}\text{-}u^k_{C2})\ i^k_g$	V^k_{opt}
2	–	V_1
1	≤0	V_2
	>0	V_3
0	–	V_4
-1	>0	V_7
	≤0	V_8
-2	–	V_9

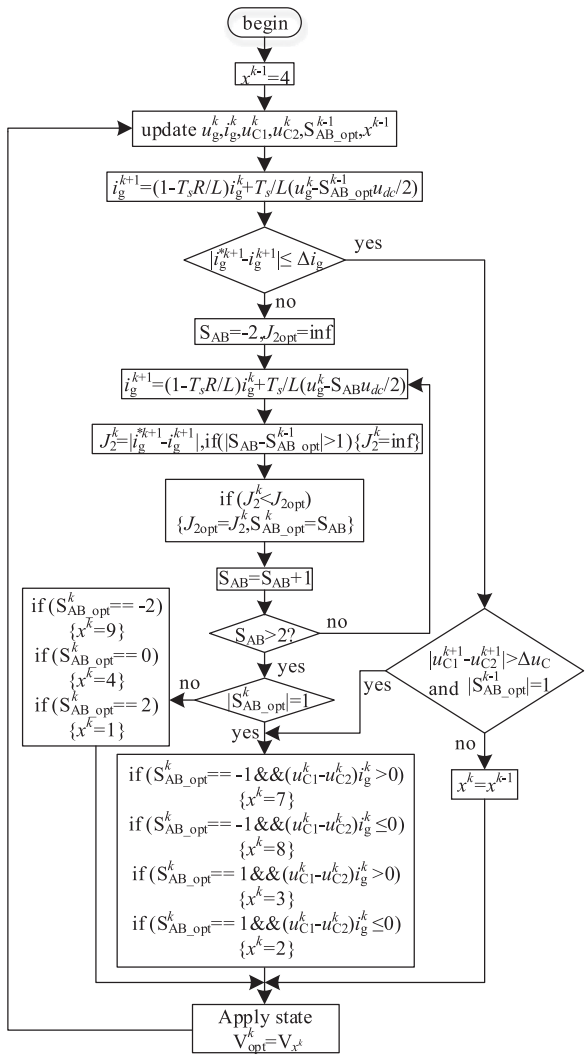

Fig. 6. Flow diagram of the proposed OS-FCS-MPC.

Step 8: Update V_{opt}^{k-1} and $S^{k-1}_{\mathrm{AB\_opt}}$, repeat steps Step 1–Step 7.

The flow diagram of the proposed OS-FCS-MPC is drawn as Fig. 6. The controller calculates the switching states at each switching interval. The continuous switching sequence obtained from Fig. 6 can ensure that the controlled variables fluctuate within a certain range and can also minimize switching losses at each switching interval. This prediction process will use the newly acquired measurements and estimates to repeat the calculations at the next moment and continue to roll forward.

This process is called a rolling optimization strategy, which provides feedback to the system and is robust to parameter changes in the predictive model.

V. Simulation and Experimental Validation

A. Simulation Results and Analysis

Simulation studies are carried out by MATLAB/Simulink software to validate the effectiveness of the proposed OS-FCS-MPC.

We use low-power experiments to approximate high-power experiments. Because high-power experiments require a lower switching frequency, we use larger inductors and capacitors than ordinary low-power experiments. The rms of ac-side voltage is 230 V and the grid frequency is 50 Hz. The output dc-voltage is 400 V and two dc-link capacitors are 1000 μF. The filter inductor is 12 mH and the filter resistance is 0.1 Ω. The dc load is four 100 Ω resistors in parallel, $N^* = 50$. Simulation results of conventional FCS-MPC are also shown as comparisons.

Since the NPC single-phase three-level PWM rectifier has a midpoint potential control target in addition to the switching frequency and current harmonics, the optimization of the midpoint potential directly affects the other two indicators.

For the same current harmonics, the higher the control accuracy requirement for the midpoint potential, the higher the switching frequency. For the same switching frequency, the higher the control accuracy requirement for the midpoint potential, the greater the current harmonic content.

Using the conventional FCS-MPC strategy for the midpoint potential control, the greater the weighting factor k_c, the higher the control priority of the midpoint potential, and the larger k_c will lead to unnecessary overoptimization of the midpoint potential, affecting the other two control targets, too small k_c will cause the midpoint voltage to run out of control, making the system lose stability and may cause overvoltage damage to the power electronics.

1) Comparing Current Harmonic Content When Their Switching Frequencies and Midpoint Potential Deviation Are Similar: Generally, the midpoint potential deviation is within 5% of the dc bus voltage, and the grid side current harmonic is within 5%. Therefore, for the OS-FCS-MPC algorithm, the midpoint potential deviation is set to $\Delta u_C = 20$ V, and the current error is set to $\Delta i_g = 2$ A. In order to compare the current harmonics of the two algorithms at the same switching frequency and midpoint potential deviation, the conventional FCS-MPC is tested to find k_c and k_n, so that the switching frequency and midpoint potential deviation of the two algorithms is close at full load, and the current harmonics are compared.

Based on the conventional FCS-MPC algorithm, the output phase voltage waveform, the ac-side current waveform, and FFT results of the ac-side current are shown as Fig. 7(a) in the full load by setting $k_c = 0.1$ and $k_n = 7$. Based on the OS-FCS-MPC algorithm, the output phase voltage waveform, the ac-side current waveform, and FFT results of the ac-side current are shown as Fig. 7(b) in the full load by setting $\Delta u_C = 20$ V and $\Delta i_g = 2$ A. Compared with Fig. 7(a) and (b), their switching frequencies and midpoint potential deviations are similar, but

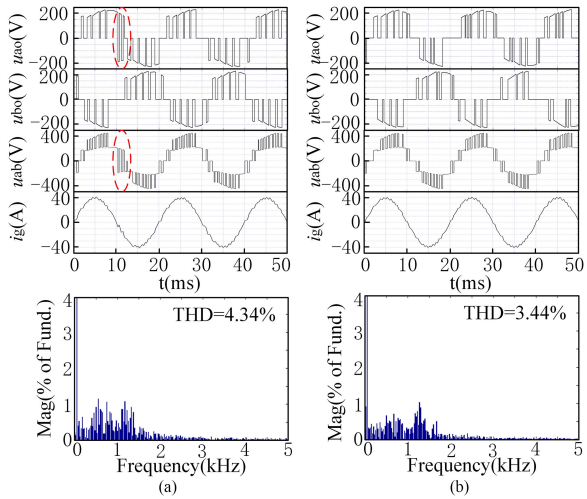

Fig. 7. Output phase voltage waveform, the ac-side current waveform, and FFT results of the ac-side current. (a) FCS-MPC full load. (b) OS-FCS-MPC full load.

the current harmonic content of the OS-FCS-MPC method is significantly lower than the FCS-MPC method. Further comparison of Fig. 7(a) and (b) shows that the phase voltage and line voltage of the conventional FCS-MPC method have jumps and that does not exist on the OS-FCS-MPC, which indicates the effectiveness of the rule of switch state switching in this article.

2) Comparing the Midpoint Potential Deviation When the Switching Frequency and Current Harmonics Are Close: The effects of parameter configuration in the two control strategies are analyzed to find the operating points, where the switching frequency and current harmonics are close when both control strategies are fully loaded.

Passed the test, it can be found that the switching frequency and the current THD of conventional FCS-MPC when $k_c = 0.03$, $k_n = 5$ are approximately the same as that of OS-FCS-MPC by setting $\Delta u_C = 20$ V and $\Delta i_g = 2$ A at full load. We compare the neutral point voltage deviation under this parameter setting, as shown in Fig. 8. When the current harmonic content and the average switching frequency of two methods are close, the neutral point voltage deviation of OS-FCS-MPC is controlled within the set range, which is significantly better than the conventional FCS-MPC algorithm.

3) Comparing Switching Frequencies, Power Loss, and Efficiency When Their Current Harmonic Content and Midpoint Potential Deviation Are Similar: Single-phase PWM rectifier losses mainly include conduction losses and switching losses. According to the FGY75N60SMD IGBT manual, the average value within the sliding window of 20 ms before the moment of the switching frequencies ($f_{\rm sw}$), switching losses power ($p_{\rm sw}$), the conduction losses power ($p_{\rm con}$), and the efficiencies (η) were calculated in the simulation.

Passed the test, it can be found that the the maximum value of midpoint potential deviation and the current THD of conventional FCS-MPC when $k_c = 0.08$, $k_n = 4.7$ are approximately the same as that of OS-FCS-MPC by setting $\Delta u_C = 20$ V and $\Delta i_g = 2$ A at full load. We compare the switching frequencies

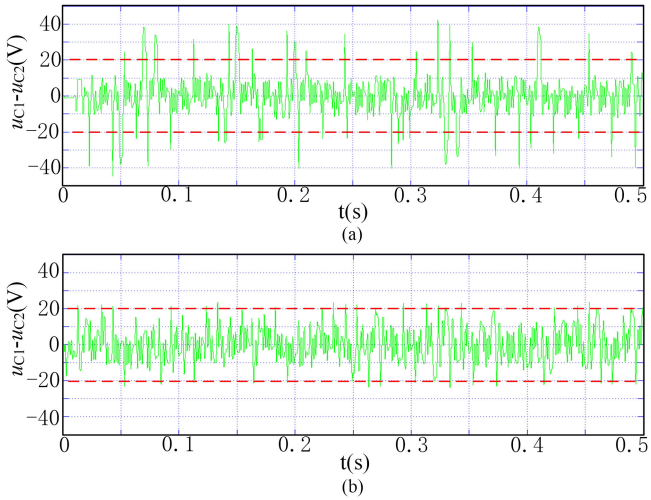

Fig. 8. Waveforms of the neutral point voltage deviation with two methods. (a) FCS-MPC full load. (b) OS-FCS-MPC full load.

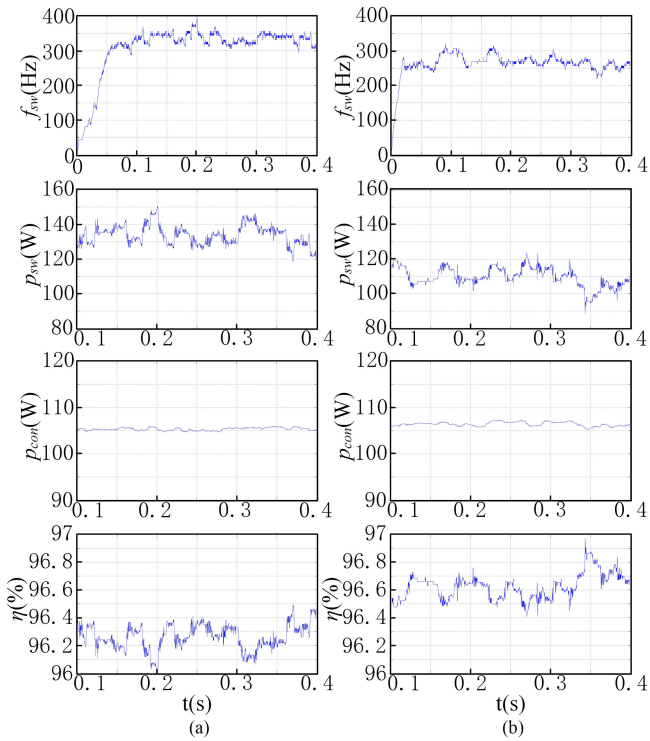

Fig. 9. Waveforms of the witching frequencies, the switching losses, conduction losses and the efficiencies with two methods. (a) FCS-MPC full load. (b) OS-FCS-MPC full load.

($f_{\rm sw}$), the switching losses ($p_{\rm sw}$), conduction losses ($p_{\rm con}$), and the efficiencies (η) under this parameter setting are shown in Fig. 9.

It can be seen from Fig. 9 that the OS-FCS-MPC conduction losses are close to the conventional FCS-MPC, the average switching frequencies and switching losses of OS-FCS-MPC are lower than the conventional FCS-MPC, and the efficiencies of OS-FCS-MPC are higher than the conventional FCS-MPC.

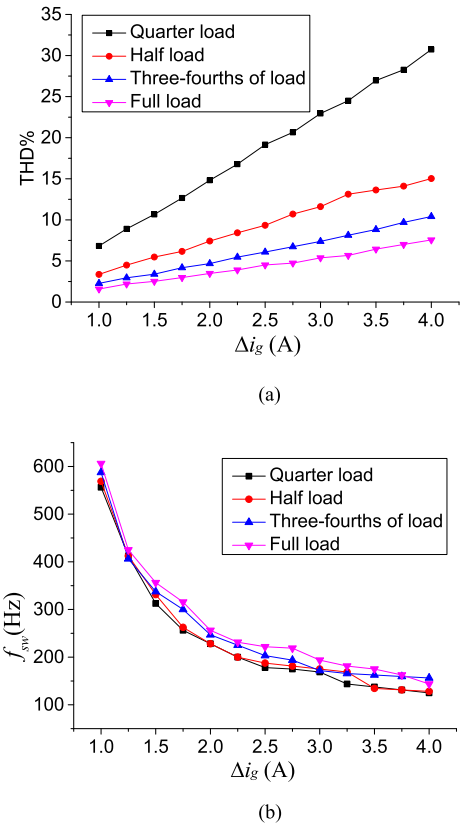

Fig. 10. Current THD and the switching frequency of OS-FCS-MPC by setting $\Delta u_C = 20$ V. (a) Current THD and Δi_g. (b) Switching frequency and Δi_g.

4) Relationship Between Δi_g and Current Harmonics and Average Switching Frequency in the OS-FCS-MPC Method: Based on the OS-FCS-MPC algorithm, the relation curves of the current THD and the average switching frequency with respect to the ac-side current deviation reference Δi_g in the different load condition are drawn as Fig. 10 by setting $\Delta u_C = 20$ V.

The average switching frequency of the system for OS-FSC-MPC has little change with the change of load when Δu_C and Δi_g are determined. In addition, the relation between the current THD and Δi_g for OS-FSC-MPC has good linearity, which is conducive to guiding the design of system parameters.

5) Parameter Sensitivity Analysis: In order to compare the influence of the parameter errors of the two control strategies, we chose a set of varying inductance values (6–24 mH) to test the two control strategies. These tests were carried out to verify the converter's steady-state THD of the grid-current and average switching frequency created from unknown filter parameters. Since the variation of the r value did not represent a problem for the MPC controller ($R << \omega L$), these variations were not registered.

Passed the test, when the conventional FCS-MPC strategy set $k_c = 0.1$, $k_n = 7$ and OS-FCS-MPC strategy set $\Delta u_C = 20$ V, $\Delta i_g = 2$ A, the midpoint potential deviation and switching frequency are close at full load. Comparing with this parameter configuration, as shown in Fig. 11, it can be seen that the OS-FCS-MPC strategy proposed in this article is significantly better than the conventional FCS-MPC strategy.

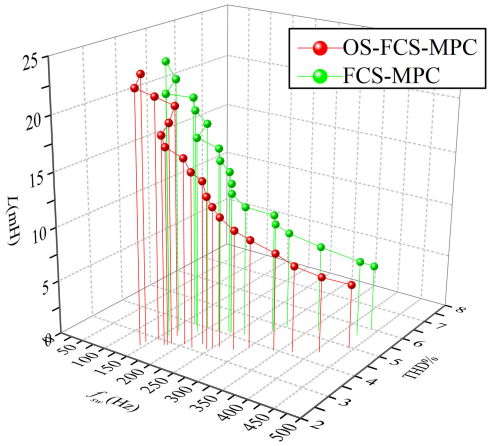

Fig. 11. Steady-state THD of the grid-current and average switching frequency under filter inductance value (unknown) variation.

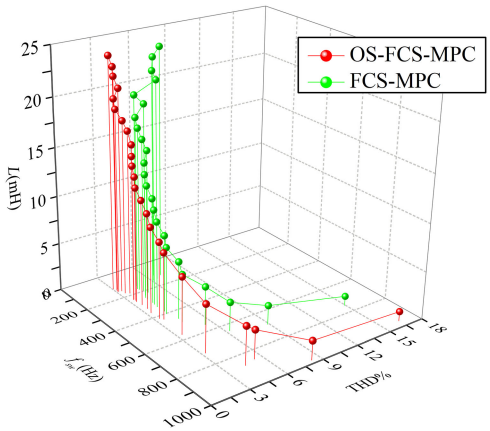

Fig. 12. Steady-state THD of the grid-current and average switching frequency under filter inductance value (known) variation.

6) Influence of Inductance Parameter Variation on Control Performance: In order to study the influence of the filter inductance value on the system control effect, this article tests the two control strategies with different inductance values (1–24 mH), where the conventional FCS-MPC strategy set $k_c = 0.1, k_n = 7$, and the OS-FCS-MPC strategy set $\Delta u_C = 20$ V, $\Delta i_g = 2$ A.

The relationship among different inductance values, switching frequency, and current THD is shown in Fig. 12. It can be seen that when the inductance value is greater than 10 mH, the OS-FCS-MPC current harmonics and switching frequency are lower than conventional FCS-MPC; when the inductance value is 2–10 mH, the OS-FCS-MPC current harmonic is lower than conventional FCS-MPC, the FCS-MPC switching frequency is lower than OS-FCS-MPC; when the inductance value is less than 2 mH, the FCS-MPC current harmonics and switching frequency are lower than OS-FCS-MPC.

B. Experimental Validation

In order to verify the effectiveness of the proposed OS-FCS-MPC control strategy, an experimental prototype of NPC single-phase three-level PWM rectifier is established as shown

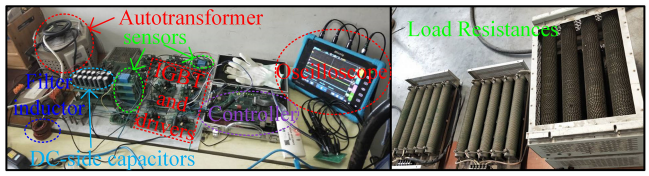

Fig. 13. Experimental setup.

in Fig. 13. The device uses a TMS320C28346 digital signal processor, FGY75N60SMD IGBT. The load resistor consists of four 100-Ω resistors. The four resistors are connected in parallel for full load. The load is changed by four air circuit-breakers controlling the number of resistors connected in parallel to the dc bus.

The parameters of the system are the same as used in simulations.

1) Comparing Current Harmonic Content When Their Switching Frequencies and Midpoint Potential Deviation Are Close: Passed the test, when the conventional FCS-MPC strategy set $k_c = 0.1$, $k_n = 7$, and OS-FCS-MPC strategy set $\Delta u_C = 20$ V, $\Delta i_g = 2$ A, the midpoint potential deviation and switching frequency are close at full load. Based on the conventional FCS-MPC algorithm, the output phase voltage waveform, the ac-side current waveform, and FFT results of the ac-side current are shown in Fig. 14 at the half and full load by setting $k_c = 0.1$ and $k_n = 7$. Based on the OS-FCS-MPC algorithm, the output phase voltage waveform, the ac-side current waveform, and FFT results of the ac-side current are also shown in Fig. 14 setting $\Delta u_C = 20$ V and $\Delta i_g = 2$ A at half load and full load.

Through graphics comparison, their switching frequencies are similar. However, the THD value of the OS-FCS-MPC method is 3.44% lower than that of the conventional FCS-MPC method at half load. The THD value of the OS-FCS-MPC method at full load is 1.03% lower than that of the conventional FCS-MPC method. It is seen that the phase voltage and line voltage of the conventional FCS-MPC method have jumps and that does not exist of the OS-FCS-MPC, which indicates the effectiveness of switching optimization in this article.

At the same time, according to Fig. 14, it is also noted that the switching frequency is higher than the half-load switching frequency when the two control strategies are fully loaded. At full load, the average switching frequency of the two control schemes is close. The half-load OS-FCS-MPC strategy switching frequency is higher than the conventional FCS-MPC strategy. When the load changes, the OS-FCS-MPC has a smaller switching frequency change than the conventional FCS-MPC.

2) Comparing the Midpoint Potential Deviation When the Switching Frequency and Current Harmonics Are Close: According to the simulation analysis, the conventional FCS-MPC method parameters are set at $k_c = 0.03$, $k_n = 5$, and the OS-FCS-MPC method parameters are set as $\Delta u_C = 20$ V and $\Delta i_g = 2$ A at full load. We compare and analyze the neutral point voltage deviation under this parameter setting, as shown in Fig. 15. The neutral point voltage deviation of OS-FCS-MPC is controlled within the set range, but the conventional FCS-MPC

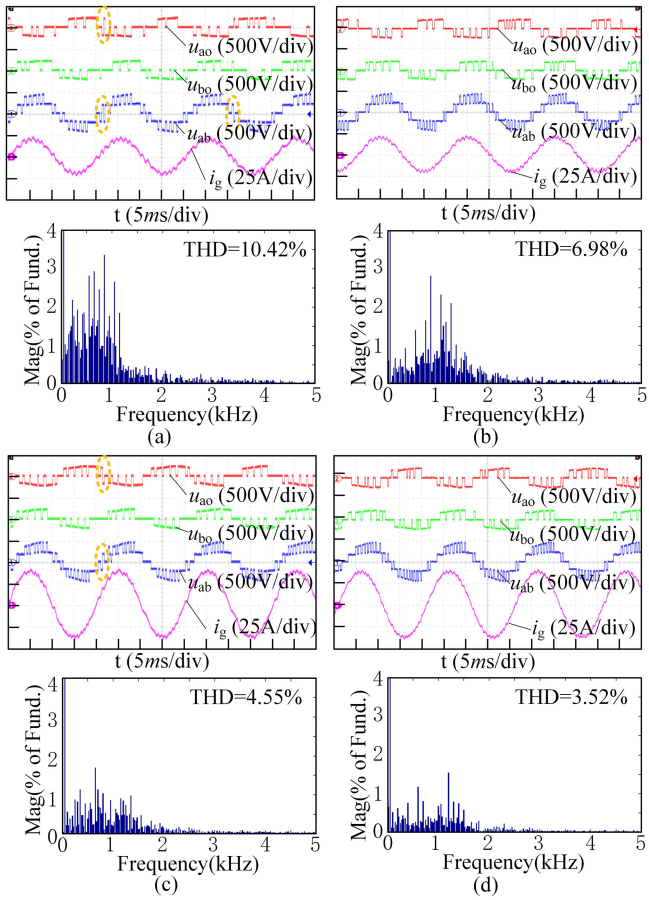

Fig. 14. Waveforms of the output phase voltage waveform, the ac-side current waveform, and FFT results of the ac-side current. (a) FCS-MPC half load. (b) OS-FCS-MPC half load. (c) FCS-MPC full load. (d) OS-FCS-MPC full load.

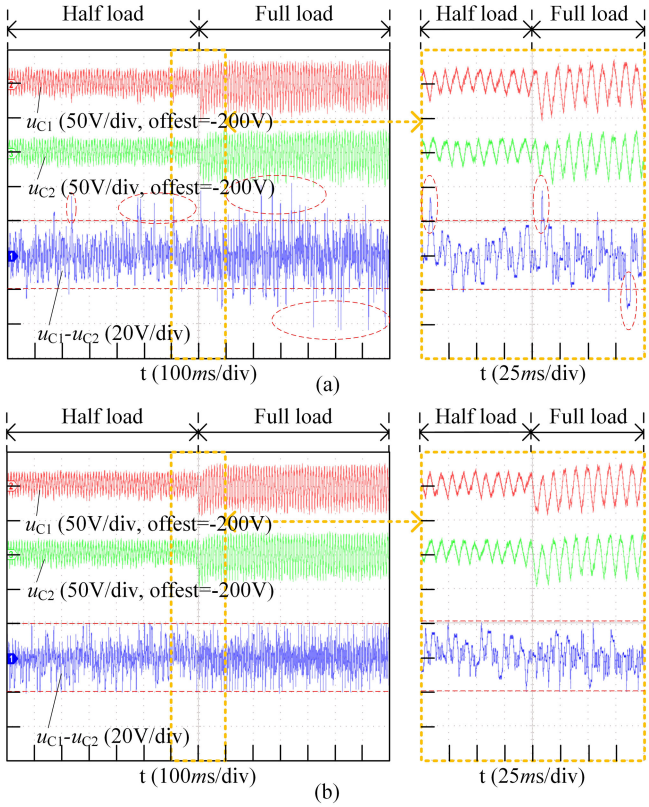

Fig. 15. Experimental waveforms of the neutral point voltage deviation. (a) FCS-MPC. (b) OS-FCS-MPC.

TABLE IV
EXPERIMENTAL DATA

Order number	k_c	k_n	Δu_C (V)	Δi_g (A)	$\lvert u_{C1}$-$u_{C2}\rvert$ (V)	f_{sw} (Hz)	THD (%)
FCS-MPC1	0.03	5	-	-	22	256	3.77
FCS-MPC2	0.1	6	-	-	21	294	3.93
FCS-MPC3	0.01	6	-	-	55	225	4.59
OS-FCS-MPC1	-	-	20	2	20	256	3.44
OS-FCS-MPC2	-	-	20	2.25	20	231	3.90
OS-FCS-MPC3	-	-	20	2.5	20	221	4.51

algorithm has multiple voltage deviation spikes, which are even twice (40 V) that of the OS-FCS-MPC.

When the current harmonic content and the average switching frequency of two methods are close, the neutral point voltage deviation of OS-FCS-MPC is controlled within the set range, which is significantly better than the conventional FCS-MPC algorithm. The correctness of the proposed scheme and the conclusion of the simulation analysis are verified.

3) Steady-State Performance Evaluation: In order to further compare the performance of the two algorithms in terms of the neutral point voltage deviation, the average switching frequency, current harmonic content. List experimental data are shown in Table IV.

Comparative analysis by Table IV, according to the data of FCS-MPC1 and OS-FCS-MPC1, the current THD value of the OS-FCS-MPC1 is lower than that of FCS-MPC1 when the neutral point voltage deviation and the average switching frequency of two methods are close. According to the data of FCS-MPC2 and OS-FCS-MPC2, the average switching frequency of the OS-FCS-MPC2 is lower than that of FCS-MPC2 when the neutral point voltage deviation and the current THD value of two methods are close. According to the data of FCS-MPC3 and OS-FCS-MPC3, the neutral point voltage deviation of the OS-FCS-MPC3 is smaller than that of FCS-MPC3 when the average switching frequency and the current THD value of two methods are close. It proves that the OS-FCS-MPC proposed in this article has better performance.

For NPC single-phase three-level PWM rectification, the steady-state performance has three core objectives, namely the grid side current harmonic content, the average switching frequency, and the midpoint potential error. Compared with the conventional FCS-MPC, the OS-FCS-MPC strategy proposed in this article is superior to the conventional FCS-MPC strategy when any two control targets are close. The conventional FCS-MPC strategy is highly coupled between the three control targets, and it is difficult to quantitatively design according to the requirements. The unreasonable parameter design will directly lead to the system not working properly and even cause equipment damage. The control strategy proposed in this article is easy to quantify the midpoint potential and current harmonics.

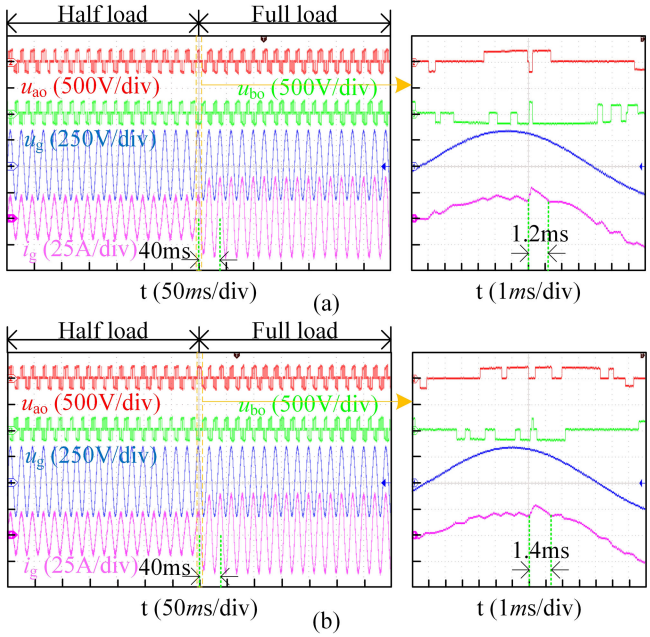

Fig. 16. Experimental waveforms of the ac-voltage and ac-current, the active power from half load to full load mutation. (a) FCS-MPC. (b) OS-FCS-MPC.

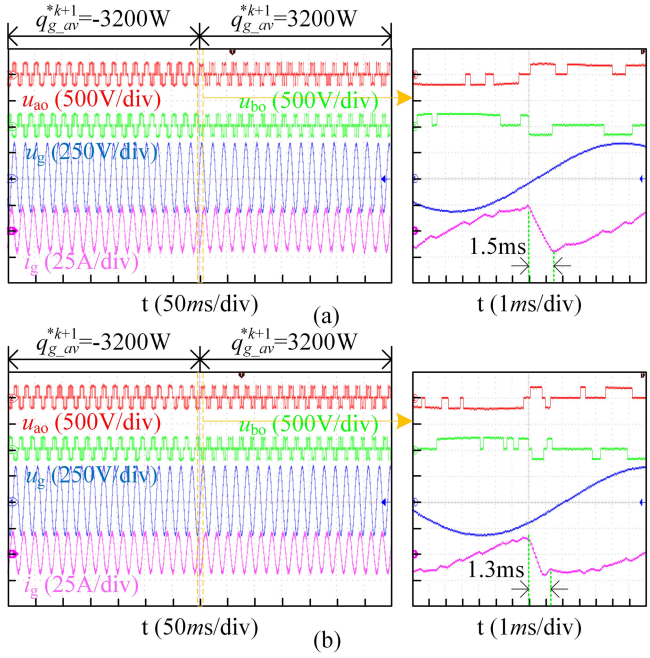

Fig. 17. Experimental waveforms of the ac-voltage and ac-current, the reactive power from –3200 to 3200 W mutation. (a) FCS-MPC. (b) OS-FCS-MPC.

4) Dynamic Performance: Fig. 16 is the experimental waveforms of the ac-voltage and ac-current of the OS-FCS-MPC and the conventional FCS-MPC algorithm from half load to full load mutation with reactive power at no load. Fig. 17 is the experimental waveforms of the ac-voltage and ac-current of the OS-FCS-MPC and conventional FCS-MPC algorithm reactive power from -3200 to 3200 W mutation with active power at no load.

When the active and reactive power changes, the current response of both algorithms has a response speed of no more than 1.5 ms. When the active power changes, the speed of the current response is much larger than the response speed of the current reference value. The tracking speed of the current amplitude of the two algorithms is almost the same, which depends mainly on the N^* parameter setting of the dc-side voltage prediction link.

VI. Conclusion

Aiming at NPC single-phase three-level PWM rectifier, a method is proposed to ensure the actual stability of the power converter by converging the ac-side current error of the single-phase PWM rectifier and the neutral point voltage of the converter to the bounded invariant set. At the same time, each performance index of the system is adjusted by setting the bounded invariant set. The novelty of the control scheme lies in that the conventional FCS-MPC of NPC single-phase three-level PWM rectifier no longer needs complicated multitarget weighting factors selection, and the required performance index can be directly realized by quantitatively setting the boundary of current error and neutral point voltage. The performance of the proposed scheme is better than the conventional FCS-MPC, which has been validated by simulation and also by experiments.

References

[1] J. Ma, W. Song, S. Wang, and X. Feng, "Model predictive direct power control for single phase three-level rectifier at low switching frequency," *IEEE Trans. Power Electron.*, vol. 33, no. 2, pp. 1050–1062, Feb. 2018.

[2] X. She, A. Q. Huang, T. Zhao, and G. Wang, "Coupling effect reduction of a voltage-balancing controller in single-phase cascaded multilevel converters," *IEEE Trans. Power Electron.*, vol. 27, no. 8, pp. 3530–3543, Aug. 2012.

[3] J. G. Hwang, P. W. Lehn, and M. Winkelnkemper, "A generalized class of stationary frame-current controllers for grid-connected AC–DC converters," *IEEE Trans. Power Del.*, vol. 25, no. 4, pp. 2742–2751, Oct. 2010.

[4] B. Crowhurst, E. F. El-Saadany, L. E. Chaar, and L. A. Lamont, "Single-phase grid-tie inverter control using DQ transform for active and reactive load power compensation," in *Proc. IEEE Int. Conf. Power Energy*, Kuala Lumpur, Sri lnaka, 2010, pp. 489–494.

[5] J. Ma, W. Song, S. Jiao, J. Zhao, and X. Feng, "Power calculation for direct power control of single-phase three-level rectifiers without phase-locked loop," *IEEE Trans. Ind. Electron.*, vol. 63, no. 5, pp. 2871–2882, May 2016.

[6] W. Song, J. Ma, L. Zhou, and X. Feng, "Deadbeat predictive power control of single-phase three-level neutral-point-clamped converters using space-vector modulation for electric railway traction," *IEEE Trans. Power Electron.*, vol. 31, no. 1, pp. 721–732, Jan. 2016.

[7] J. Rodriguez and P. Cortes, "Predictive control of a three-phase neutral-point clamped inverter," in *Proc. IEEE Predictive Control Power Converters Elect. Drives*, 2012, pp. 65–79.

[8] Z. Zhang, M. T. Larijani, W. Tian, X. Gao, J. Rodríguez, and R. Kennel, "Long-horizon predictive current control of modular-multilevel converter HVDC systems," in *Proc. IECON 43rd Annu. Conf. IEEE Ind. Electron. Soc.*, Beijing, China, 2017, pp. 4524–4530.

[9] Z. Zhang, F. Wang, J. Wang, J. Rodríguez, and R. Kennel, "Nonlinear direct control for three-level NPC back-to-back converter PMSG wind turbine systems: Experimental assessment with FPGA," *IEEE Trans. Ind. Informat.*, vol. 13, no. 3, pp. 1172–1183, Jun. 2017.

[10] F. Wang *et al.*, "Finite control set model predictive torque control of induction machine with a robust adaptive observer," *IEEE Trans. Ind. Electron.*, vol. 64, no. 4, pp. 2631–2641, Apr. 2017.

[11] S. Vazquez, A. Marquez, J. I. Leon, L. G. Franquelo, and T. Geyer, "FCS-MPC and observer design for a VSI with output LC filter and sinusoidal output currents," in *Proc. 11th IEEE Int. Conf. Compat., Power Electron. Power Eng.*, Cadiz, Spain, 2017, pp. 677–682.

[12] M. Siami, D. A. Khaburi, M. Rivera, and J. Rodríguez, "A computationally efficient lookup table based FCS-MPC for PMSM drives fed by matrix converters," *IEEE Trans. Ind. Electron.*, vol. 64, no. 10, pp. 7645–7654, Oct. 2017.

[13] P. Karamanakos and T. Geyer, "Model predictive torque and flux control minimizing current distortions," *IEEE Trans. Power Electron.*, vol. 34, no. 3, pp. 2007–2012, Mar. 2019.

[14] K. G. Pavlou, M. Vasiladiotis, and S. N. Manias, "Constrained model predictive control strategy for single-phase switch-mode rectifiers," *IET Power Electron.*, vol. 5, no. 1, pp. 31–40, Jan. 2012.

[15] P. Acuna, R. P. Aguilera, A. M. Y. M. Ghias, M. Rivera, C. R. Baier, and V. G. Agelidis, "Cascade-free model predictive control for single-phase grid-connected power converters," *IEEE Trans. Ind. Electron.*, vol. 64, no. 1, pp. 285–294, Jan. 2017.

[16] R. P. Aguilera and D. E. Quevedo, "On stability of finite control set MPC strategy for multicell converters," in *Proc. IEEE Int. Conf. Ind. Technol.*, Vina del Mar, Chile, 2010, pp. 1277–1282.

[17] R. P. Aguilera and D. E. Quevedo, "On stability and performance of finite control set MPC for power converters," in *Proc. Workshop Predictive Control Elect. Drives Power Electron.*, Munich, Germany, 2011, pp. 55–62.

[18] T. Geyer, R. P. Aguilera, and D. E. Quevedo, "On the stability and robustness of model predictive direct current control," in *Proc. IEEE Int. Conf. Ind. Technol.*, Cape Town, South Africa, 2013, pp. 374–379.

[19] D. E. Quevedo, J. A. De Dona, and G. C. Goodwin, "On the dynamics of receding horizon linear quadratic finite alphabet control loops," in *Proc. 41st IEEE Conf. Decis. Control*, Las Vegas, NV, USA, 2002, pp. 2929–2934, vol. 3.

[20] S. Vazquez, J. Rodriguez, M. Rivera, L. G. Franquelo, and M. Norambuena, "Model predictive control for power converters and drives: Advances and trends," *IEEE Trans. Ind. Electron.*, vol. 64, no. 2, pp. 935–947, Feb. 2017.

[21] C. A. Rojas, J. Rodriguez, F. Villarroel, J. R. Espinoza, C. A. Silva, and M. Trincado, "Predictive torque and flux control without weighting factors," *IEEE Trans. Ind. Electron.*, vol. 60, no. 2, pp. 681–690, Feb. 2013.

[22] M. Siami, H. K. Savadkoohi, A. Abbaszadeh, D. A. Khaburi, J. Rodriguez, and M. Rivera, "Predictive torque control of a permanent magnet synchronous motor fed by a matrix converter without weighting factor," in *Proc. 7th Power Electron. Drive Syst. Technol. Conf.*, Tehran, Iran, 2016, pp. 614–619.

[23] L. Guo, K. Zhang, N. Jin, L. Cao, K. Luo, and H. Wang, "Dynamic cost function based predictive torque control for permanent magnet synchronous motor without using weighting factor," in *Proc. IEEE Int. Power Electron. Appl. Conf. Expo.*, Shenzhen, China, 2018, pp. 1–5.

[24] F. Wang, H. Xie, Q. Chen, S. A. Davari, J. Rodriguez, and R. Kennel, "Parallel predictive torque control for induction machines without weighting factors," *IEEE Trans. Power Electron.*, vol. 35, no. 2, pp. 1779–1788, Feb. 2020.

[25] Y. Zhang and H. Yang, "Model-predictive flux control of induction motor drives with switching instant optimization," *IEEE Trans. Energy Convers.*, vol. 30, no. 3, pp. 1113–1122, Sep. 2015.

[26] Y. Zhang and H. Yang, "Two-vector-based model predictive torque control without weighting factors for induction motor drives," *IEEE Trans. Power Electron.*, vol. 31, no. 2, pp. 1381–1390, Feb. 2016.

[27] M. Xiao, T. Shi, Y. Yan, W. Xu, and C. Xia, "Predictive torque control of permanent magnet synchronous motors using flux vector," *IEEE Trans. Ind. Appl.*, vol. 54, no. 5, pp. 4437–4446, Sep./Oct. 2018.

[28] R. E. K. Meesala, V. P. K. Kunisetti, and V. K. Thippiripati, "Enhanced predictive torque control for open end winding induction motor drive without weighting factor assignment," *IEEE Trans. Power Electron.*, vol. 34, no. 1, pp. 503–513, Jan. 2019.

[29] P. G. Ipoum-Ngome, D. L. Mon-Nzongo, J. Song-Manguelle, R. C. C. Flesch, and T. Jin, "Optimal finite state predictive direct torque control without weighting factors for motor drive applications," *IET Power Electron.*, vol. 12, no. 6, pp. 1434–1444, 2019.

[30] Y. Yang, H. Wen, M. Fan, M. Xie, and R. Chen, "Fast finite-switching-state model predictive control method without weighting factors for T-type three-level three-phase inverters," *IEEE Trans. Ind. Informat.*, vol. 15, no. 3, pp. 1298–1310, Mar. 2019.

[31] R. P. Aguilera and D. E. Quevedo, "Predictive control of power converters: Designs with guaranteed performance," *IEEE Trans. Ind. Informat.*, vol. 11, no. 1, pp. 53–63, Feb. 2015.

[32] C. A. Rojas, J. R. Rodriguez, S. Kouro, and F. Villarroel, "Multiobjective fuzzy-decision-making predictive torque control for an induction motor drive," *IEEE Trans. Power Electron.*, vol. 32, no. 8, pp. 6245–6260, Aug. 2017.

Xu Zhang was born in Liaoning, China, in 1990. He received the B.S. and M.S degrees in electrical engineering and automation from the China University of Mining and Technology, Xuzhou, China, in 2014 and 2017, respectively. He is currently working toward the Ph.D. degree in electrical engineering with the School of Electrical and Power Engineering, China University of Mining and Technology.

His main research interests include power electronics, multilevel converter, data drive control, intelligent algorithm, and system optimization.

Guojun Tan (Member, IEEE) was born in Zunyi, Guizhou, China, in 1962. He received the Ph.D. degree in motor driver and its automation from the China University of Mining and Technology, Xuzhou, China, in 1992.

Since 2000, he has been a Professor with the School of Information and Electrical Engineering, China University of Mining and Technology, where he has been the Chief Professor of National Key Discipline on power electronics and motor driver since 2003. His main research interests include electrical drive, intelligent algorithm, and system optimization.

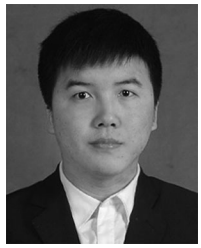

Tao Xia was born in Gansu Province, China. He received the B.S. degree in electrical engineering and automation from Jilin University, Jilin, China, in 2014. He is currently working toward the master's degree in electrical engineering with the School of Electrical and Power Engineering, China University of Mining and Technology, Xuzhou, China.

His research interests include grid synchronization technology, and power converter control.

Qiang Wang was born in Xuzhou, Jiangsu, China, in 1996. He received the B.S. degree in 2018 from the Sun Yue-Qi Honors College of China University of Mining and Technology (CUMT), China, where he is currently working toward the Ph.D. degree in electrical engineering with the School of Electrical and Power Engineering.

His current research interests include reliability in power electronics and systems, including reliable assessment and multiphysics modeling of power electronic devices and converters.

Xiang Wu was born in Jiangsu, China, in 1990. He received the B.S. and Ph.D. degrees in electrical engineering and automation from the China University of Mining and Technology, Xuzhou, China, in 2013 and 2019, respectively.

He is currently a Lecturer of power electronics and electrical drives with the School of Electrical and Power Engineering, China University of Mining and Technology, Xuzhou, China. His research interests include power electronics, modern control theory, battery management system, and motor drives.